ACS OMEGA

Open Access

http://pubs.acs.org/journal/acsodf

Article

Synthesis of Graphene and Graphene Films with Minimal Structural Defects

Minh-Hai Tran, Ian Booth, Arash Azarakhshi, Peter Berrang, Jeremy Wulff, and Alexandre G. Brolo*

Cite This: *ACS Omega* 2023, 8, 40387−40395

Read Online

ACCESS | Metrics & More | Article Recommendations

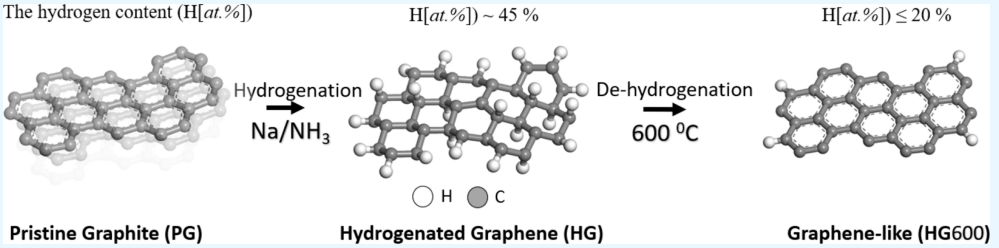

ABSTRACT: Graphene is a carbon material with extraordinary properties that has been drawing a significant amount of attention in the recent decade. High-quality graphene can be produced by different methods, such as epitaxial growth, chemical vapor deposition, and micromechanical exfoliation. The reduced graphene oxide route is, however, the only current approach that leads to the large-scale production of graphene materials at a reasonable cost. Unfortunately, graphene oxide reduction normally yields graphene materials with a high defect density. Here, we introduce a new route for the large-scale synthesis of graphene that minimizes the creation of structural defects. The method involves high-quality hydrogen functionalization of graphite followed by thermal dehydrogenation. We also demonstrated that the hydrogenated graphene synthesis route can be used for the preparation of high-quality graphene films on glass substrates. A reliable method for the preparation of these types of films is essential for the widespread implementation of graphene devices. The structural evolution from the hydrogenated form to graphene, as well as the quality of the materials and films, was carefully evaluated by Raman spectroscopy.

INTRODUCTION

Graphene, a monolayer of delaminated graphite, is a two-dimensional material of sp^2-bonded carbon that has remarkable electronic, optical, and mechanical properties due to its special electronic semimetal band structure in which conduction and valence bands meet at the Dirac point.[1−5] In particular, this electronic condition confers the high mobility of charge carriers with unique electrical conductivity properties combined with optical transparency. These characteristics of graphene have attracted tremendous interest for applications in electronics, photonics, and energy storage.[6−11]

In principle, graphene can be fabricated by simply delaminating a single graphite layer, one of the cheapest and most abundant resources in the world. This type of single-layer graphene is useful for specialized fundamental research, such as investigations of the quantum properties of the material.[5,6,10] Nevertheless, industrial applications require bulk graphene materials and high-quality films. It is important to emphasize that the standalone single-layered graphene cannot resist aggregation due to the van der Waals interactions between carbon rings. This effect and further instabilities due to thermal fluctuations have led to the conclusion that long-range crystalline order in graphene is impossible to maintain at room temperature.[12,13]

Therefore, bulk graphene materials and films consist of a distribution of exfoliated graphitic forms with an average "small" number of stacked layers. The production of large amounts of these materials either in bulk or as large area films of high quality is very challenging. Although significant advances on the various graphene fabrication methods, including mechanical exfoliation, liquid-phase exfoliation, bottom-up synthesis, and reduction of graphene oxide, are constantly being reported,[13−18] there has not yet been a universal method that can meet the industrial requirements criteria in both material quality and fabrication yield.[19] According to a 2021 review on graphene synthesis by Santhiran et al.,[15] there are several limiting aspects to large industrial production through the current graphene preparation routes. Those limitations are relative to costs, availability of resources, and the requirement for complex technologies.

Received: July 4, 2023
Accepted: September 7, 2023
Published: October 18, 2023

For instance, the exfoliation route, either the mechanical or liquid phase, does not scale-up. Furthermore, some bottom-up methods, including chemical vapor synthesis and epitaxial growth, require complex facilities to deal with high vacuum, heating requirements, and complex gas systems.[15]

The production of graphene-like materials through graphene oxide reduction is the most common route for large-scale fabrication. In this case, the production cost for graphene oxide is low, and the reaction can be processed under 100 °C in ambient conditions.[15,16] Unfortunately, large-scale graphene oxide production involves strong oxidation precursors, such as fuming nitric acid and potassium chlorate, leading to a high risk of explosion.[15,16] Moreover, the subsequent reduction processes lead to the rupture of the graphene lattice via formation of CO_2, leaving permanent vacancy and hole defects in the resulting materials or films.[20,21] The presence of a high density of defects influences not only the electrical and thermal conductivities of the material but also the mechanical strength that relies on the sp^2 lattice structure of graphene.[20,21]

It is then important to consider alternative synthetic methods that can produce graphene materials and films on a large scale while minimizing the defects in the structure of the product. In this contribution, we report on a new route for the synthesis of graphene that follows hydrogen functionalization of graphite instead of oxidation. The method described here allowed the coating of large-area glass substrates with a good level of chemical homogeneity. The structure of fully hydrogenated graphene, known as graphane, was predicted theoretically in 2007.[22] Afterward, since 2009, there have been several attempts to fabricate hydrogenated graphene by microwave discharge,[23] plasma,[24] chemical vapor deposition[25] or using super critical hydrogen at high pressure and high temperature in a diamond anvil cell.[26] However, those methods are suitable only on a small scale in microgram quantities or for the formation of graphane films. Although electrochemical reduction has shown the ability to hydrogenated bulk quantities of graphene, this method still has the drawback of unexpected chemical functionalizing from the electrolyte and typically produces a low hydrogenation ratio.[27,28] The hydrogenation of carbon materials through solvated electrons from dissolved alkali metals in ammonia, also known as the Birch reduction,[29] is considered the most capable of producing bulk quantities of graphane. However, safety considerations are an important concern, since lithium is the most common metal used for that reaction.[30−32] Although the hydrogenation efficiency obtained by Birch reduction is generally higher compared to either physical or electrochemical methods, this method still has a disadvantage in that the residues from lithium salt are hard to remove due to the strong interactions between lithium atoms and graphene layers[33] which can be seen in Fourier transformed infrared absorption spectroscopy (FTIR) by the sharp peak at about 3600 cm^{-1}.[30] A few groups tackled this challenge by replacing lithium with sodium in Birch reduction, but only micrograms of hydrogenated carbon was produced[34,35] due to the violent reaction. Morse et al.[36] have reported a more practical route to scale-up the production of hydrogenated carbon, but the degree of hydrogenation needed improvements since a residual graphite crystalline peak was present in the X-ray diffraction (XRD) of their product.

Density functional theory calculations were used to model graphane. The computational data indicated a C−H bond dissociation energy (BDE) in the range of about 3.5−4.0 eV.[37] In contrast, graphene oxide has different BDEs for the various oxygen functional groups. Some of the approximated values are 6.0, 4.8, and 10.5 eV for C−OOH, C−OH and C−O−C, respectively.[38] Thus, while thermal reduction of graphite oxide requires high temperatures of about 1000 °C,[39] hydrogenated graphite (HG) should be thermally stripped of hydrogen functional groups at lower temperatures, around 500−600 °C.

An attempt to overcome the current limitations of traditional Birch reduction is reported in this work. A modified route to graphite hydrogenation is suggested, leading to both high quality and quantity of the obtained product. It is also shown that thermal dehydrogenation leads to good-quality graphene films on glass substrates, which is an important step for the implementation of devices. The dehydrogenation of graphane can then be considered a better route for bulk graphene production compared with the graphene oxide method. The dehydrogenation route is amenable to scale-up, and it also maintains the sp^2 structure of the final graphene product better than the oxidation process, due to the low temperature requirements.

EXPERIMENTAL SECTION

Sample Preparation. *Warning:* The ingredients in the Birch reduction include liquid ammonia and alkali metals, requiring considerable safety awareness due to the risk of explosion. The use of face shield, blast shield, and fume hood are essential requirements. This reaction should only be performed by adequately trained personnel and monitored at all the times.

Graphite powder (synthetic, 20 μm diameter) from Sigma-Aldrich was used for the Birch reduction method.[32,36] Typically, a mixture of dry ice and acetone (−78 °C) was used to cool a three-neck flask fitted to a condenser. Liquid ammonia (150 mL) was condensed into the flask followed by the slow addition of sodium (20 g) and graphite powder (5 g). The mixture was stirred for 1.5 h, and then a protonation step was initiated by the dropwise addition of 200 mL of butanol and methanol to the reaction for more than 3 h. The ammonia was then allowed to evaporate overnight. The samples of carbon materials produced by this procedure were rinsed three times with methanol, deionized water, and dilute sulfuric acid followed by sonication and vacuum filtering to remove any remaining sodium impurities. The sample was then dried in an oven at 125 °C for 24 h. The dried powder of HG materials obtained by this procedure will be termed HG throughout this manuscript. The dehydrogenation step of the processes was accomplished by thermal annealing at either 500 °C (for 3 h) or 600 °C (for 3 h). In both cases, the temperature was increased at a 10 °C/min rate in Argon gas. The samples obtained after annealing are referred to as HG500 and HG600.

Characterization. Microscale images of the powder samples were obtained by scanning electron microscopy (SEM, Hitachi S-4800 FESEM). The extent of the chemical functionalization of the samples was inferred by FTIR (PerkinElmer Spectrum Two). The component phase purity and the crystalline structures of the samples were obtained by XRD (Panalytical Empyrean X-ray diffractometer) of 2θ with CuKa radiation λ = 0.1542 nm, 40 kV tube voltage, 40 mA tube current with scanning range of 10−60°.

Raman spectroscopy was performed using a Renishaw 1000 Raman microscope. The samples were excited using a 532-nm laser focused to ∼2 μm diameter spot with a 50× (NA = 0.75) objective lens. The laser intensity was adjusted between 300

https://doi.org/10.1021/acsomega.3c04788
ACS Omega 2023, 8, 40387−40395

and 500 μW to minimize any adverse heating effect. The laser light was rejected by a bandpass filter, and the Raman scattering was measured in a spectrograph equipped with a CCD camera. Samples for the Raman measurements were prepared by drop coating a (1 wt %) methanol solution of the carbon material (sonication was required to ensure dispersion) on a glass slide. The glass slide was dried at room temperature before the Raman measurements. Spectra were recorded from 5 to 10 spots randomly chosen from each sample.

Raman mappings were utilized to verify the homogeneity of the chemical characteristics of graphene films formed through the thermal reduction of HG. The films were prepared as follows: The dispersion of hydrogenated graphene in deionized water was dropped on a glass substrate, and then the films were heated at 600 °C for 3 h in Argon gas (HG600 films). The Raman maps were obtained over an area of 32.5 μm by 32.5 μm (0.5 μm step) using 532 nm laser, 1.75 mW for 5 s and 3 accumulations. Several areas, chosen randomly, were mapped in a given film to provide statistics of long-range chemical homogeneity. A MATLAB code employed a 2 Gaussian method to fit the Raman bands. All spectra were corrected by a linear baseline between 1050 and 1800 cm^{-1}. The hydrogen content (H[atom %]) was estimated based on the slope of the linear baseline (m) divided by G-band intensity ($I(G)$), according to eq 1 below.[40,41]

$$\mathrm{H[atom\ \%]} = 21.7 + 16.6\log\left\{\frac{m}{I(G)}[\mu\mathrm{m}]\right\} \quad (1)$$

This Raman method for the determination of H[atom %] was shown to be accurate in determining hydrogenated carbon material for H[atom %] > 20%.

RESULTS AND DISCUSSION

Figure 1 shows the representative FTIR spectra of the samples produced in this work. Figure 1a corresponds to the spectra from the precursor graphite (PG), Figure 1b is the HG material, and Figure 1c,d are spectra of the HG material after thermal treatment at 500 and 600 °C, respectively. The HG sample in Figure 1b has a significant sharp peak at 2850 cm^{-1} that is assigned to the sp^3-hybridized C−H stretching vibration.[32] The presence of that peak is a strong indication of successful hydrogen functionalization of the original graphitic structure. The FTIR spectra of the thermally treated samples, HG500 and HG600, shown in Figure 1c,d, do not present any characteristic peak, consistent with a functional group-free structure. The disappearance of the C−H stretching band in the FTIR spectra of the HG carbon material after the moderate annealing process demonstrates effective dehydrogenation at relatively mild temperatures.

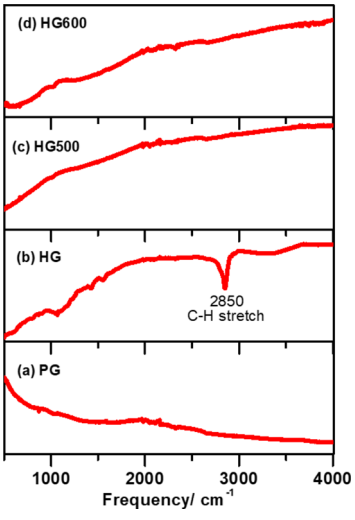

Figure 1. FTIR spectra of (a) precursor graphite (PG), (b) hydrogenated graphite (HG), and thermally treated samples at (c) 500 °C (HG500) and (d) 600 °C (HG600) samples.

The degree of graphitization and the crystallinity parameters were characterized by XRD. Figure 2a presents a XRD pattern that is characteristic for graphite, with a peak at 26.5° of the lattice (002) and the derivative interlayer spacing (d_{002}) of 0.34 nm calculated using Bragg's law.[42,43] The graphite (PG) XRD at 26.5° shifts to 18.9° for HG, as shown in Figure 2b. The interlayer distance calculated from the pattern in Figure 2b was 0.47 nm. That is smaller than the 0.8 nm layer distance typically obtained from XRD of graphene oxide[43] and larger than pristine graphite (PG) (0.34 nm). It is possible to attribute the difference in layer distances to the presence of covalently bound hydrogen atoms on the surface of exfoliated graphene.[32] The XRD patterns of the thermally treated samples HG500 and HG600 are shown in Figure 2c,d, respectively. The main peaks for Figure 2c,d are closer to those observed for graphite in Figure 2a. The approximately 26.0° diffraction feature observed in Figure 2c,d, relative to the 26.5° observed in Figure 2a, suggests dehydrogenation and restoration of sp^2-conjugated domains. These results indicate the restacking in a turbostratic carbon structure which is less dense than the graphite precursor.[44]

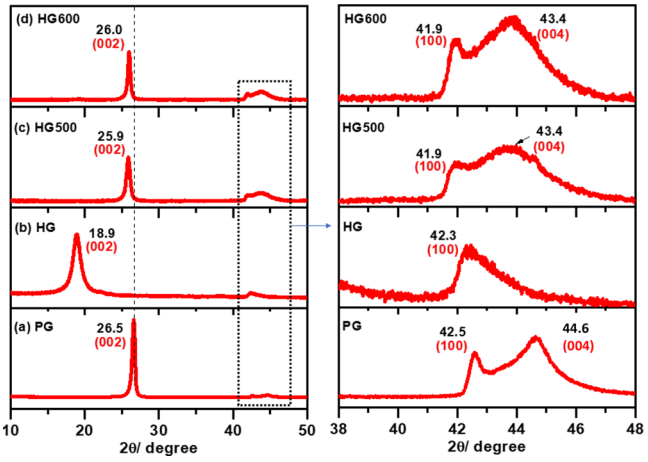

Figure 2. XRD analysis of (a) graphite, (b) hydrogenated graphite, and (c) and (d) samples thermal annealed at 500 and 600 °C, respectively. The diffractograms on the right show a magnified image of the XRD spectra in the range about 40−50°.

The diffraction peak in Figure 2 at around 44°, assigned to (004) planes, indicates that both the number of parallel carbon layers and the order of aromatic carbon grid has recovered after thermal reduction.[42] It is important to note that the (004) peak was not recovered in graphene films produced by thermally reduced graphene oxide.[43,45] On the other hand, that feature clearly starts to emerge in Figure 2 after a relatively mild thermal treatment of 500 °C. These results suggest that both crystallinity and ordering layers were recovered more

https://doi.org/10.1021/acsomega.3c04788
ACS Omega 2023, 8, 40387−40395

efficiently by following the annealing of hydrogenated materials than from the oxide reduction route.

The crystalline structure parameters of the samples were also calculated based on two specific planes, (002) and (100), corresponding to XRD peaks at around 26 and 42°, respectively.[42,51]

The interlayer spacing (d_{002}) was determined by Bragg's eq 2, the graphitization degree (g) by Franklin's eq 3, the crystallite size (L_a) and stacking height (L_c) from Scherrer's eq 4, and the number of layers (n) were determined by eq 5.

$$d_{002} = \lambda/2\sin\theta_{002} \quad (2)$$

$$g = [(0.3440 - d_{002})/(0.3440 - 0.3354)] \times 100\% \quad (3)$$

$$L_a = k_1\lambda/[\beta_{100}\cos\theta_{100}] \text{ and } n = L_c = k_2\lambda/[\beta_{002}\cos\theta_{002}] \quad (4)$$

$$n = L_c/d_{002} \quad (5)$$

where k is the Scherrer parameter (k_1 = 1.84, k_2 = 0.94), β and θ represent the full width at half-maximum (fwhm) and the Bragg angle of the diffraction peak, respectively. The values of 0.3440 and 0.3354 are assumed as the carbon layer spacing (nm) of the original carbonaceous materials and of an ideal graphite crystal.[42]

The summary of the structural parameters of all samples is displayed in Table 1. Table 1 shows that hydrogenation

Table 1. Crystallinity Properties Calculated from XRD Spectra of Pristine Graphite and Hydrogenated Graphene Derivatives

sample	d_{002} (nm)	g (%)	L_a (nm)	L_c (nm)	n
PG	0.335	100	86	742	2215
HG	0.467	13.7	30	146	313
HG500	0.343	13.1	56	298	869
HG600	0.342	22.2	68	466	1363

affected approximately 80% of the stacked structure of graphitization (g). However, up to 79% of the graphene crystallinity was recovered in HG600 based on the values of crystalline size (L_a). In contrast, similar quality graphene obtained from the thermal graphene oxide route requires thermal conditions above 1000 °C.[43] These are expected results, since the favored energetics allow the recovery of the crystallinity of graphene structure by thermal treatment at lower temperature for the hydrogenated route compared to the oxidized material. Table 1 also shows that the number of layers (n) of HG decreased almost seven times from the PG material, suggesting an increase in detached graphene sheets promoted by the inserted hydrogens. The thermal reduction toward graphene leads to an increase of the numbers of layers (n) in HG500 and HG600 (Table 1) to approximately half of the value in the graphite precursor (PG). The variation in the values of n indicated in Table 1 is supported by the scanning electron micrographs presented in Figure 3.

Representative SEM images of the samples in Figure 3 show that the original graphite material (PG) was mainly composed of large particles with a significant number of stacked layers (Figure 3a). Clearly separated layers with porous structures can be observed in Figure 3b for the HG sample. The thermally treated (500 and 600 °C) samples, HG500 and HG600, present similar appearance in Figure 3c,d, with more wrinkled and thinner-layered structures. Overall, the results in

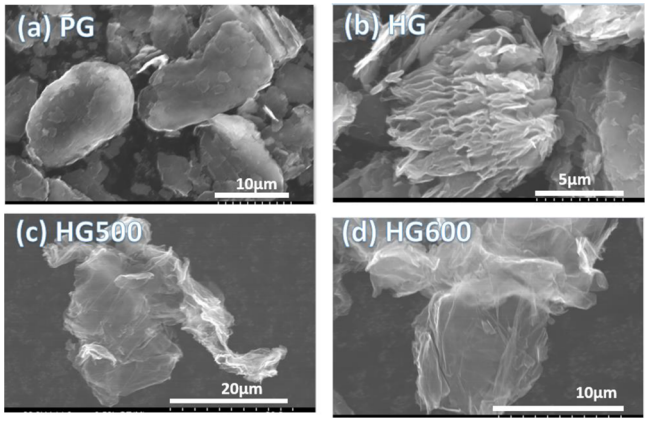

Figure 3. SEM images of samples: (a) PG, (b) HG, (c) HG500, and (d) HG600.

Figure 3 demonstrate that the dehydrogenation process, followed by thermal treatment, significantly reduced the thickness of the bundle of graphite layers in the material.

Raman spectroscopy is the most commonly used technique for the characterization of graphene-type materials. It is a well-known versatile tool for the determination of the number and orientation of graphene layers, as well as the level of disorder and functionalization in graphene-based materials.[46−51] The characteristic Raman G-band (at ∼1600 cm^{-1}) is assigned to the E_{2g} phonon at the Γ-point of the Brillouin zone, while the 2D-band at the second phonon zone (∼2700 cm^{-1}) is due to transverse optical (TO) phonons around the K-point in the Brillouin zone.[52] The D-band (at ∼1300 cm^{-1}) arises from an excitation of a phonon induced by a defect in the double resonance process around the K-point.[53,54] The 2D band, which is a second-order overtone of the D-band, is a Raman feature induced by defects. However, it does not originate from defects and, as a result, does not serve as an indicator of defect presence.[53] Instead, the Raman 2D-band shape is used as a fingerprint for the number of graphene layers and it is very dependent on the electronic band structure of graphene.[55,56] Accordingly, based on the characteristics of the peaks in both regions of the first and second phonon Raman scattering (D and 2D), the defects and graphitic structure quality can be evaluated.

Figure 4 shows the evolution of the Raman signature from the precursor material PG (Figure 4a), through the hydrogenation product HG (Figure 4b) to the thermally dehydrogenated samples HG500 and HG600 (Figure 4c,d, respectively).

The interpretation of the Raman features of the hydrogenated and dehydrogenated materials presented in Figure 4 takes into account the Raman signatures for tetrahedral amorphous carbon[59,60] compared to the Raman of functionalized carbon species, such as graphene oxide.[58,61]

The Raman spectrum for PG in Figure 4a is typical for graphite, with prominent features assigned to the G-band (∼1580 cm^{-1}) and the 2D-band (∼2700 cm^{-1}) characteristic for sp^2 carbon networks. A weak D-band that originates from the edge of the graphite domains is also present in Figure 4a.[54] Other minor peaks that originate from the combination of phonon and overtones are assigned to the D + D″ (∼2400 cm^{-1}) and 2 D′ (∼3200 cm^{-1}) which are related to two phonon scattering processes that do not require defects for activation.[50,63,64]

https://doi.org/10.1021/acsomega.3c04788
ACS Omega 2023, 8, 40387−40395

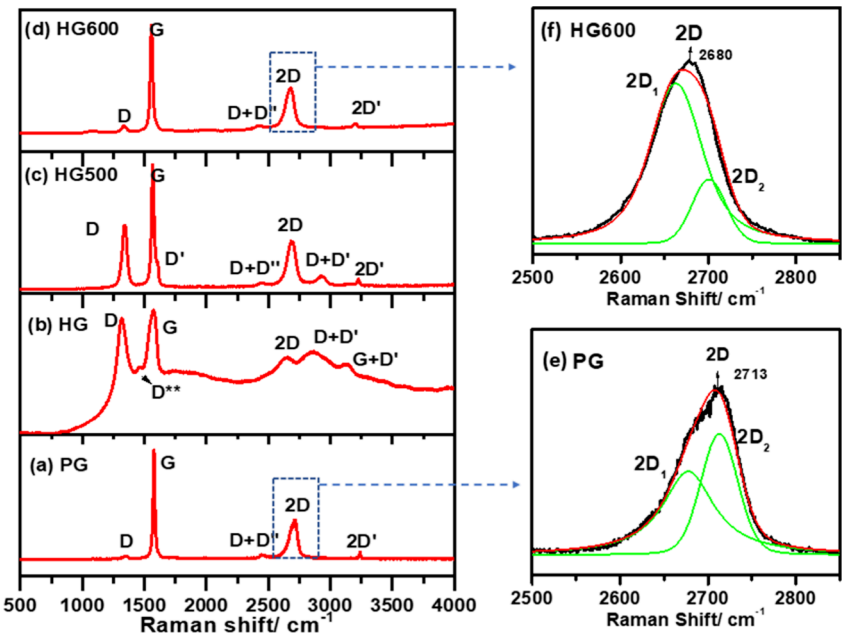

Figure 4. Raman spectra of (a) pristine graphite (PG) (b) hydrogenated graphite (HG), (c, d) baked sample at 500 °C (HG500) and 600 °C (HG600), respectively; (e, f) deconvolution of 2D peak of PG and HG600, respectively.

After hydrogenation, the Raman features of the HG sample, displayed in Figure 4b, are significantly different in terms of featured bands and spectral shape relative to the PG shown in Figure 4a. The Raman photoluminescence background in Figure 4b is a typical signature of hydrogenated carbon samples and it is assigned to the hydrogen saturation of nonradiative recombination centers.[42,65] The magnitude of the background is related to the hydrogenation levels; for instance, samples with less than 20 atom % of hydrogenation were shown to not exhibit a photoluminescent background.[42] Figure 4b shows the appearance of a new D** band at ∼1500 cm^{-1}, which possibly can be assigned to the contribution of C−H vibrations in hydrogenated carbons[58] or to the reduction in the number of layer[66] due to the intercalation of hydrogen functionalization. Considered as a whole, the Raman features in Figure 4b are signatures of a hydrogenated graphene structure. The Raman data corroborate the FTIR and XRD results discussed in Figures 1 and 2, respectively. Furthermore, the hydrogenation promoted an increase in the defect-induced D-band, as shown in Figure 4b. The double-phonon area has also changed from a high-intensity 2D band observed in Figure 4a to triple bands assigned to 2D (∼2650 cm^{-1}), D+ D′ (∼2900 cm^{-1}) and G+ D′ (∼3130 cm^{-1}) in Figure 4b. The triple bands in the second-phonon region (between ∼2650 and 3131 cm^{-1}) are similar to some Raman features reported for graphene oxide, where those peaks illustrate the disruption of the graphitic structure and the D+ D′ (also assigned as D + G band) and G+ D′ band that arise due to lattice disorder and defects.[61,63,67] A broad feature in that region was also proposed as evidence that nanocrystalline graphite had been transformed into low sp^3 amorphous carbon.[59]

The Raman spectrum of the HG500 sample in Figure 4c presents features previously assigned to graphene or nanocrystalline graphene structure.[60,67] There are several defect-induced bands including the D-band (∼1350 cm^{-1}), the D′-band (∼1615 cm^{-1}) and their combination, and the D+ D′-band (∼2970 cm^{-1}). In particular, the D-band is assigned to a breathing mode at the K-point while the D′-band corresponds to an intravalley double resonance process which is activated by the presence of defects.[61] The defects allow combination of intervalley phonon processes that produces the D+ D′-band.[50] The small band at around 1000 cm^{-1} in Figure 4c is labeled as a D*-band, representing a disordered graphitic lattice involving a mixture of sp^2 and sp^3 carbons.[58] The thermal treatment removed the photoluminescence background and increased the intensity of the 2D-band. The increase of the 2D peak activity, around 2700 cm^{-1}, compared to the other peaks in the second phonon region (∼ 2300 to 3300 cm^{-1}) strongly supports the decrease in the density of hydrogen groups on the graphitic structure, since that band is sensitive to π-structure of graphene.[57]

A typical Raman spectrum of the carbon sample dehydrogenated at a higher temperature (HG600) is presented in Figure 4d. Overall, the Raman features of the HG600 product (Figure 4d) present characteristics similar to those of the precursor graphite (Figure 4a). Most of the defect-induced bands are not present in the spectrum of Figure 4d, which is dominated by major peaks in the G- and 2D-band regions. This result proves the recovery of the graphitic structure after thermal treatment of the HG samples. The shape and position of the 2D-band are sensitive to the number of graphene layers. Figure 4e and f present an expanded view of the 2D region for precursor PG and HG600 sample, respectively. The peaks in the 2D region were fitted by Lorentzian line shapes. The 2D-band in bulk graphite (PG, Figure 4e) consists of two components: $2D_1$ and $2D_2$, at approximately 2695 and 2735 cm^{-1}, respectively. Compared to the graphite peak in Figure 4e, HG600 has the component peak of $2D_1$ that is more dominant exhibiting in Figure 4f. It has been demonstrated that as the number of graphene layers decreases to below 5, the relative intensity of the lower frequency peak, $2D_1$, increases progressively relative to the $2D_2$-peak.[56,68] The deconvolution of the contribution from the $2D_1$ to the overall 2D-band, presented in Figure 4e,f, indicates that thermally treated hydrogenated graphene sample HG600 has fewer stacked layers than PG. Furthermore, the restored graphitic structure

https://doi.org/10.1021/acsomega.3c04788
ACS Omega 2023, 8, 40387−40395

after dehydrogenation of the HG product (HG600) can be classified as restacked graphene layers with random stacking known as turbostratic graphite.[69] The absence of an interlayer interaction between the graphene planes in turbostratic graphite yields a Raman signature that is similar to that observed from a monolayer graphene but with larger line width.[70] This is consistent with the more symmetric shape of the broad feature in Figure 4f compared to that in Figure 4e due to the blue shift of the 2D band.

While the changes in the Raman spectrum of graphene oxide under the reduction are normally considered in the first resonant range, the Raman spectra of hydrogenated graphene before and after the reduction process have significant differences in the second resonance range. It should be noted that the 2D band is sensitive to the π-band structure.[57] The oxidation process normally causes ring opening and formation of carboxylic groups resulting in the destruction of the conjugated system.[20,57] This means that graphene synthesized through the reduced graphene oxide route inherits in-plane vacancy defects from the graphene oxide precursor. These defects are readily evident in the Raman signature of the material by the suppressed 2D band.[58]

In summary, graphene oxide and hydrogenated graphene have quite similar Raman bands except for the fluorescence effect observed for the hydrogenated case. The intensity ratio of the D- and G-bands is about 1 and the triple bands are in the second resonance range for both materials. The HG samples produced here are well functionalized on graphene sheets and lead to disordered graphene structures upon annealing.

Raman spectroscopy was used to characterize defects and crystalline structures in the hydrogenated graphene derivatives. Three distinct kinds of defects, namely on-site defects, hopping, and Coulomb defects, are possible in the electron-defect scattering model.[53] Specifically, hydrogen bonding to a carbon atom in the graphene sheet is considered as a type of on-site defect, while hopping defect is described as vacancies in the graphene structure.[48,49,53] The main defect-induced Raman features are the D-band at 1350 cm^{-1} and the D′-band at 1625 cm^{-1}. The characteristics of those features were proved to be proportional to the concentration and type of defects.[49,53] The Coulomb defect, also referred to as charged impurities, is not expected to exert the same influence on the D- and D′-bands.[48] In fact, the intensity of the D-band is expected to increase with the defect density while the D′-band intensity stays constant.[48] Therefore, the ratio of the integrated intensities from the D- and D′-bands can be used to define the origin of the defects.[48] The convergence of the D′-band with the G-band is observed at elevated levels of defect concentrations.[48] This phenomenon accounts for the nonexistence of a distinct D′-band in the HG600 sample depicted in Figure 4d. On the other hand, both the D- and D′-bands are present in Figure 4c for the HG500 sample. The integrated intensity ratio of D and D′ (I_D/I_D') calculated from Figure 4c was 11.8. This value is close to the I_D/I_D' = 13 expected for sp^3 defect type as described by Eckmann et al.[48,63] In the case of graphane (HG), shown in Figure 4b, the D-band is attributed to the stretch motion of the $C(sp^3)-C(sp^3)$ bonds or the wagging motion of the $C(sp^3)-H$ bond and the D′-band is due to the wagging motion of $C(sp^3)-H$ bonds on hydrogenated graphene.[46] The analysis of the Raman data suggests a partly dehydrogenated process for the HG samples annealed at 500 °C. A more efficient dehydrogenation occurred at higher temperature (600 °C), as evidenced by the decreasing intensities of both D- and D′-bands in HG600, suggesting that the reduction process is more efficient at higher temperatures. The HG sample in Figure 4a exhibits a D**-band around 1500 cm^{-1} that is related to sp^3 carbon hybridization.[58]

The well-known Tuinstra and Koenig relation (ratio of the D- to G-band intensities (I_D/I_G))[51] is commonly used to quantify disorder or determine the crystalline quality of graphene. The I_D/I_G-value is expected to vary inversely with the crystallite size (L_a) or the distance between the defects (L_D). These are opposite trends in terms of quality.[51,62] However, second-order bands can be used to supplement the crystalline quality information for graphene-based materials.[62] In particular, the ratios of the second phonon bands (2D, D+D′) to the G-band change in the opposite way; I_{2D}/I_G show an increase for increased crystallinity, while I_{D+D}'/I_G show a decrease as demonstrated by Vollebregt.[62] The various ratios of the Raman spectra of the HG samples in Figure 4 are listed in Table 2. The resulting trends demonstrated an increase in crystalline structure quality of HG samples after thermal annealing, particularly at higher temperature.

Table 2. Comparison of Ratios of Raman Peaks of Pristine Graphite and Hydrogenated Graphene Derivatives

sample	$I\left(\frac{2D}{G}\right)$	$I\left(\frac{D+D'}{G}\right)$
PG	0.3	0
HG	0.2	0.3
HG500	0.3	0.1
HG600	0.5	0

The results from Raman and XRD data presented in Figures 2 and 4 indicate that the HG route is more viable for the preparation of graphene-like materials than the graphene oxide approach, since it allows for large-scale graphene synthesis with lower temperature and less disordered structure. Hydrogen can intercalate into graphene layers and break van der Waals forces (as oxygen does), but the hydrogenated material can be reduced more efficiently than oxygen functional groups to yield graphene sheets.

Finally, the HG samples were coated on glass substrates to obtain graphene-like films upon annealing. The films were Raman mapped (196 Raman spectra each); i.e., the laser was rastered across the film. The mappings were used to obtain some information about the chemical homogeneity resulting from both the hydrogenation and annealing processes. Figure 5 shows the results of Raman mapping distribution histograms of hydrogen content, calculated using eq 1, from individual Raman spectra for HG films deposited on glass substrates. The Raman mapping results in Figure 5a,b exhibit a uniform color, demonstrating that the HG films adhered well before and after annealing on a glass substrate, maintaining a relatively uniform spatial composition. Figure 5c shows that the distribution of hydrogen contents for the HG film was about 45% with a spatial variation of about 3−5%. On the other hand, the histogram for the annealed sample, HG600, showed a sharp peak of 20%. Notice that Raman spectroscopy is used in Figure 5 to determine the level of hydrogenation of the films based on a method that correlates hydrogenation with the background fluorescence in hydrogenated materials.[42] That method, however, has a minimum limit of hydrogenation level estimation at ∼ 20 atom %, i.e., films with H% ≤ 20% are

https://doi.org/10.1021/acsomega.3c04788
ACS Omega 2023, 8, 40387−40395

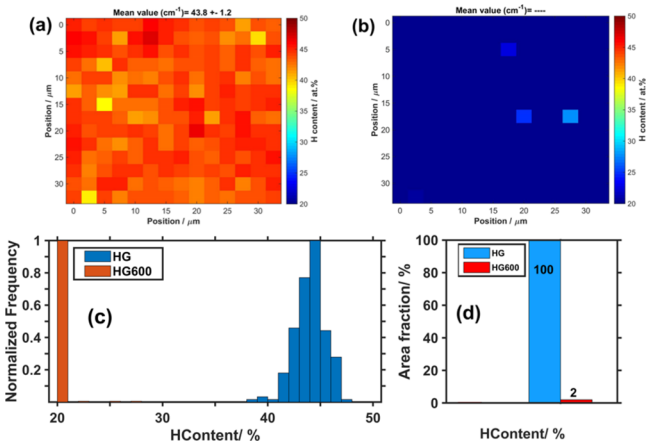

Figure 5. Raman mapping of (a) HG and (b) HG600. Comparisons of hydrogen content (%) relative to (c) normalized frequency and (d) area fraction.

indistinguishable. The results for the annealed sample, Figure 5d, imply then that ~98% of the film coated on a glass substrate contains less than 20% H content after annealing. These results, combined with the features discussed in Figure 4, point toward very effective dehydrogenation and graphene-like characteristics for annealed graphene (HG) films coated on glass substrate. The uniformity of HG and HG600 samples on the glass can be explained by the fact that the polar surface of glass is suitable for the dispersion of HG in water, facilitating a more uniform coverage of the glass. Optimization of the deposition process (through, for instance, different solvents) might be a path to improve the quality of the graphene-like films formed on metal surfaces. In any case, the important aspect is that the hydrogenated graphene allowed the preparation of a uniform graphene film on glass by annealing at a much lower thermal condition (600 °C) than that for the graphene oxide route (~800 to 1000 °C).

CONCLUSIONS

In summary, the present work has demonstrated a new route to produce graphene and graphene coatings by the thermal treatment of hydrogenated carbon materials (graphane). This approach overcomes the inherent shortcomings of the graphene oxide method in restoring the pi−pi conjugation of the graphene structure. This means that materials and films with fewer defects can be fabricated. The hydrogen groups in graphene also assist in the preparation of uniform films covering polar substrates such as glass, which is essential for the synthesis of graphene-based films for device applications.

AUTHOR INFORMATION

Corresponding Author

Alexandre G. Brolo − *Department of Chemistry, University of Victoria, Victoria, BC V8W 3 V6, Canada; Center for Advanced Materials and Related Technologies, University of Victoria, Victoria, BC V8W 2Y2, Canada; Department of Physics and Astronomy, University of Victoria, Victoria, BC V8W 2Y2, Canada;* orcid.org/0000-0002-3162-0881; Email: agbrolo@uvic.ca

Authors

Minh-Hai Tran − *Department of Chemistry, University of Victoria, Victoria, BC V8W 3 V6, Canada; Center for Advanced Materials and Related Technologies, University of Victoria, Victoria, BC V8W 2Y2, Canada;* orcid.org/0000-0003-4658-4956

Ian Booth − *XlynX Materials Inc, Sidney, BC V8L 3R6, Canada*

Arash Azarakhshi − *Center for Advanced Materials and Related Technologies, University of Victoria, Victoria, BC V8W 2Y2, Canada; Department of Physics and Astronomy, University of Victoria, Victoria, BC V8W 2Y2, Canada*

Peter Berrang − *XlynX Materials Inc, Sidney, BC V8L 3R6, Canada*

Jeremy Wulff − *Department of Chemistry, University of Victoria, Victoria, BC V8W 3 V6, Canada; Center for Advanced Materials and Related Technologies, University of Victoria, Victoria, BC V8W 2Y2, Canada;* orcid.org/0000-0001-9670-160X

Complete contact information is available at: https://pubs.acs.org/10.1021/acsomega.3c04788

Notes

The authors declare no competing financial interest.

ACKNOWLEDGMENTS

This work was funded by the MITACS Accelerate Program.

REFERENCES

(1) Geim, A. K.; Novoselov, K. S. The Rise of Graphene. *Nat. Mater.* **2007**, *6*, 183−191.

(2) Wallace, P. R. The Band Theory of Graphite. *Phys. Rev.* **1947**, *71*, 622−634.

(3) Geim, A. K. Graphene: Status and Prospects. *Science* **2009**, *324*, 1530−1534.

(4) Bolotin, K. I.; Sikes, K. J.; Jiang, Z.; Klima, M.; Fudenberg, G.; Hone, J.; Kim, P.; Stormer, H. L. Ultrahigh Electron Mobility in Suspended Graphene. *Solid State Commun.* **2008**, *146*, 351−355.

(5) Novoselov, K. S.; Geim, A. K.; Morozov, S. V.; Jiang, D.; Katsnelson, M. I.; Grigorieva, I. V.; Dubonos, S. V.; Firsov, A. A. Two-Dimensional Gas of Massless Dirac Fermions in Graphene. *Nature* **2005**, *438*, 197−200.

(6) Ando, T. Anomaly of Optical Phonon in Monolayer Graphene. *J. Phys. Soc. Jpn.* **2006**, *75*, 124701−124701.

(7) Zhamu, A.; Chai, S. H.; Jang, Z. B. Dense Graphene Balls for Hydrogen Storage. US20200317524A1, 2020.

(8) Bunch, J. S.; Zande, A. M. V. D.; Verbridge, S. S.; Frank, I. W.; Tanenbaum, D. M.; Parpia, J. M.; Craighead, H. G.; Mceuen, P. L. Electromechanical Resonators from Graphene Sheets. *Science* **2007**, 490−493.

(9) Tsang, C. H. A.; Huang, H.; Xuan, J.; Wang, H.; Leung, D. Y. C. Graphene Materials in Green Energy Applications: Recent Development and Future Perspective. *Renew. Sustainable Energy Rev.* **2020**, *120*, No. 109656.

(10) Eliel, G. S. N.; Moutinho, M. V. O.; Gadelha, A. C.; Righi, A.; Campos, L. C.; Ribeiro, H. B.; Chiu, P. W.; Watanabe, K.; Taniguchi, T.; Puech, P.; Paillet, M.; Michel, T.; Venezuela, P.; Pimenta, M. A. Intralayer and Interlayer Electron-Phonon Interactions in Twisted Graphene Heterostructures. *Nat. Commun.* **2018**, *9*, 1221.

(11) Zhang, Y.; Jiang, Z.; Small, J. P.; Purewal, M. S.; Tan, Y. W.; Fazlollahi, M.; Chudow, J. D.; Jaszczak, J. A.; Stormer, H. L.; Kim, P. Landau-Level Splitting in Graphene in High Magnetic Fields. *Phys. Rev. Lett.* **2006**, *96*, No. 136806.

(12) Atif, R.; Inam, F. Reasons and Remedies for the Agglomeration of Multilayered Graphene and Carbon Nanotubes in Polymers. *Beilstein J. Nanotechnol.* **2016**, *7*, 1174−1196.

(13) Avouris, P.; Dimitrakopoulos, C. Graphene: Synthesis and Applications. *Mater. Today* **2012**, *15*, 86−97.

(14) Guo, S.; Dong, S. Graphene Nanosheet: Synthesis, Molecular Engineering, Thin Film, Hybrids, and Energy and Analytical Applications. *Chem. Soc. Rev.* **2011**, *40*, 2644−2672.
(15) Santhiran, A.; Lyngaran, P.; Abinan, P.; Kuganathan, N. Graphene Synthesis and Its Recent Advances in Applications—A Review. *Carbon* **2021**, *7*, 76.
(16) Adetayo, A.; Runsewe, D. Synthesis and Fabrication of Graphene and Graphene Oxide: A Review. *Open J. Compos. Mater.* **2019**, *9*, 207−229.
(17) Bhuyan, M. S. A.; Uddin, M. N.; Islam, M. M.; Bipasha, F. A.; Hossain, S. S. Synthesis of Graphene. *Int. Nano Lett.* **2016**, *6*, 65−83.
(18) Shinde, P. V.; Singh, M. K. Synthesis, Characterization, and Properties of Graphene Analogs of 2D Material. In *Fundamentals and Sensing Applications of 2D Materials*; Woodhead Publishing, 2019, pp. 91−143.
(19) Raccichini, R.; Varzi, A.; Passerini, S.; Scrosati, B. The Role of Graphene for Electrochemical Energy Storage. *Nat. Mater.* **2015**, *14* (3), 271−279.
(20) Feicht, P.; Eigler, S. Defects in Graphene Oxide as Structural Motifs. *ChemNanoMat* **2018**, *4* (3), 244−252.
(21) Banhart, F.; Kotakoski, J.; Krasheninnikov, A. V. Structural Defects in Graphene. *ACS Nano* **2011**, *5* (1), 26−41.
(22) Sofo, J. O.; Chaudhari, A. S.; Barber, G. D. Graphane: A Two-Dimensional Hydrocarbon. *Phys. Rev. B* **2007**, *75*, No. 153401.
(23) Khare, B. N.; Meyyappan, M.; Cassell, A. M.; Nguyen, C. V.; Han, J. Functionalization of Carbon Nanotubes Using Atomic Hydrogen from a Glow Discharge. *Nano Lett.* **2002**, *2* (1), 73−77.
(24) Elias, D. C.; Nair, R. R.; Mohiuddin, T. M. G.; Morozov, S. V.; Blake, P.; Halsall, M. P.; et al. Control of Graphene's Properties by Reversible Hydrogenation: Evidence for Graphane. *Science* **2009**, *323* (5914), 610−613.
(25) Burgess, J. S.; Matis, B. R.; Robinson, J. T.; Bulat, F. A.; Keith Perkins, F.; Houston, B. H.; Baldwin, J. W. Tuning the Electronic Properties of Graphene by Hydrogenation in a Plasma Enhanced Chemical Vapor Deposition Reactor. *Carbon* **2011**, *49* (13), 4420−4426.
(26) Smith, D.; Howie, R. T.; Crowe, I. F.; Simionescu, C. L.; Muryn, C.; Vishnyakov, V.; Novoselov, K. S.; Kim, Y.-J.; Halsall, M. P.; Gregoryanz, E.; Proctor, J. E. Hydrogenation of Graphene by Reaction at High Pressure and High Temperature. *ACS Nano* **2015**, *9* (8), 8279−8283.
(27) Daniels, K. M.; Daas, B. K.; Srivastava, N.; Williams, C.; Feenstra, R. M.; Sudarshan, T. S.; Chandrashekhar, M. V. S. Evidences of Electrochemical Graphene Functionalization and Substrate Dependence by Raman and Scanning Tunneling Spectroscopies. *J. Appl. Phys.* **2012**, *111* (11), No. 114306.
(28) Zhao, M.; Guo, X.-Y.; Ambacher, O.; Nebel, C. E.; Hoffmann, R. Electrochemical Generation of Hydrogenated Graphene Flakes. *Carbon* **2015**, *83*, 128−135.
(29) Birch, A. J. 117. Reduction by Dissolving Metals. Part I. *J. Chem. Soc.* **1944**, 430−436.
(30) Schäfer, R. A.; Englert, J. M.; Wehrfritz, P.; Bauer, W.; Hauke, F.; Seyller, T.; Hirsch, A. On the Way to Graphane—Pronounced Fluorescence of Polyhydrogenated Graphene. *Angew. Chem., Int. Ed.* **2013**, *52* (2), 754−757.
(31) Bouša, D.; Luxa, J.; Sedmidubský, D.; Huber, Š.; Jankovský, O.; Pumera, M.; Sofer, Z. Nanosized Graphane (C1H1.14)n by Hydrogenation of Carbon Nanofibers by Birch Reduction Method. *RSC Adv.* **2016**, *6* (8), 6475−6485.
(32) Yang, Z.; Sun, Y.; Alemany, L. B.; Narayanan, T. N.; Billups, W. E. Birch Reduction of Graphite Edge and Interior Functionalization by Hydrogen. *J. Am. Chem. Soc.* **2012**, *134* (45), 18689−18694.
(33) Emery, N.; Hérold, C.; Lagrange, P. Overview on the Intercalation Reactions of Lithium Alloys into Graphite. *Prog. Solid State Chem.* **2008**, *36* (3), 213−222.
(34) Subrahmanyam, K. S.; Kumar, P.; Maitra, U.; Govindaraj, A.; Hembram, K. P. S. S.; Waghmare, U. V.; Rao, C. N. R. Chemical Storage of Hydrogen in Few-layer Graphene. *Proc. Natl. Acad. Sci. U. S. A.* **2011**, *108* (7), 2674.
(35) Eng, A. Y. S.; Sofer, Z.; Huber, Š.; Bouša, D.; Maryško, M.; Pumera, M. Hydrogenated Graphenes by Birch Reduction: Influence of Electron and Proton Sources on Hydrogenation Efficiency, Magnetism, and Electrochemistry. *Chem.—Eur. J.* **2015**, *21* (47), 16828−16838.
(36) Morse, J. R.; Zugell, D. A.; Matis, B. R.; Willauer, H. D.; Balow, R. B.; Baldwin, J. W. Macroscale Evaluation and Testing of Chemically Hydrogenated Graphene for Hydrogen Storage Applications. *Int. J. Hydrog. Energy* **2020**, *45* (3), 2135−2144.
(37) Tao, S.; Liu, H.-T.; Yan, L.-M.; Yue, B.-H.; Li, A.-J. Hydrogenation of Graphene Nanoflakes and C−H bond Dissociation of Hydrogenated Graphene Nanoflakes: a Density Functional Theory Study. *Adv. Manuf.* **2017**, *5* (3), 289−298.
(38) Hassan, W. M. I.; Verma, A.; Nekovei, R.; Jeyakumar, R.; Khader, M. M. Theoretical Investigation of the Oxygen Bond Dissociation Energies in Graphene Oxide. In *2015 IEEE Nanotechnology Materials and Devices Conference (NMDC)*; IEEE, 2015, pp. 1−2.
(39) Jankovský, O.; Sedmidubský, D.; Lojka, M.; Sofer, Z. *Thermal Properties of Graphite Oxide, Thermally Reduced Graphene and Chemically Reduced Graphene*. In AIP Conference Proceedings; AIP Publishing, 2017, Vol. *1866*, 1.
(40) Buijnsters, J. G.; Gago, R.; Jiménez, I.; Camero, M.; Agulló-Rueda, F.; Gómez-Aleixandre, C. Hydrogen Quantification in Hydrogenated Amorphous Carbon Films by Infrared, Raman, and X-ray Absorption Near Edge Spectroscopies. *J. Appl. Phys.* **2009**, *105* (9), No. 093510.
(41) Casiraghi, C.; Piazza, F.; Ferrari, A. C.; Grambole, D.; Robertson, J. Bonding in Hydrogenated Diamond-like Carbon by Raman Spectroscopy. *Diam. Relat. Mater.* **2005**, *14* (3), 1098−1102.
(42) Qiu, T.; Yang, J.-G.; Bai, X.-J.; Wang, Y.-L. The Preparation of Synthetic Graphite Materials with Hierarchical Pores from Lignite by One-step Impregnation and their Characterization as Dye Absorbents. *RSC Adv.* **2019**, *9* (22), 12737−12746.
(43) Huh, S. H. Thermal Reduction of Graphene Oxide. In *Physics and Applications of Graphene: Experiments*, 1st ed.; Sergey, M., Ed.; Intech Open: London, 2011; pp. 5−90.
(44) Ōya, A.; Marsh, H. Phenomena of Catalytic Graphitization. *J. Mater. Sci.* **1982**, *17* (2), 309−322.
(45) Minh-Hai, T.; Kyung, H. J. Economical Thermal Reduction of Graphite Oxide for Supercapacitor Applications. *New Phys.: Sae Mulli* **2017**, *67*, 333−337.
(46) Zhou, X. H.; Huang, Y.; Chen, X. S.; Lu, W. Density Functional Theory Study of the Vibrational Properties of Hydrogenated Graphene. *Solid State Commun.* **2013**, *57*, 24−28.
(47) Sharma, M.; Rani, S.; Pathak, K. D.; Bhatia, R.; Kumar, R.; Sameera, I. Temperature Dependent Raman Modes of Reduced Graphene Oxide: Effect of Anharmonicity, Crystallite Size and Defects. *Carbon* **2021**, *184*, 437−444.
(48) Eckmann, A.; Felten, A.; Mishchenko, A.; Britnell, L.; Krupke, R.; Novoselov, K. S.; Casiraghi, C. Probing the Nature of Defects in Graphene by Raman Spectroscopy. *Nano Lett.* **2012**, *12* (8), 3925−3930.
(49) López-Díaz, D.; Delgado-Notario, J. A.; Clericò, V.; Diez, E.; Merchán, M. D.; Velázquez, M. M. Towards Understanding the Raman Spectrum of Graphene Oxide: The Effect of the Chemical Composition. *Coatings* **2020**, *10*, 524.
(50) Ferrari, A. C.; Basko, D. M. Raman Spectroscopy as a Versatile Tool for Studying the Properties of Graphene. *Nat. Nanotechnol.* **2013**, *8* (4), 235−246.
(51) Ferrari, A. C. Raman Spectroscopy of Graphene and Graphite: Disorder, Electron−Phonon Coupling, Doping and Nonadiabatic Effects. *Solid State Commun.* **2007**, *143* (1−2), 47−57.
(52) Merlen, A.; Buijnsters, J. G.; Pardanaud, C. A Guide to and Review of the Use of Multiwavelength Raman Spectroscopy for Characterizing Defective Aromatic Carbon Solids: from Graphene to Amorphous Carbons. *Coatings* **2017**, *7* (10), 153.
(53) Venezuela, P.; Lazzeri, M.; Mauri, F. Theory of Double-Resonant Raman Spectra in Graphene: Intensity and Line Shape of

https://doi.org/10.1021/acsomega.3c04788
ACS Omega 2023, 8, 40387−40395

Defect-Induced and Two-Phonon Bands. *Phys. Rev. B* **2011**, *84* (3), No. 035433.
(54) Pimenta, M. A.; Dresselhaus, G.; Dresselhaus, M. S.; Cançado, L. G.; Jorio, A.; Saito, R. Studying Disorder in Graphite-based Systems by Raman Spectroscopy. *Phys. Chem. Chem. Phys.* **2007**, *9* (11), 1276−1290.
(55) Rao, R.; Tishler, D.; Katoch, J.; Ishigami, M. Multiphonon Raman Scattering in Graphene. *Phys. Rev. B* **2011**, *84* (11), No. 113406.
(56) Ferrari, A. C.; Meyer, J.; Scardaci, V.; Casiraghi, C.; Lazzeri, M.; Mauri, F.; Piscanec, S.; Jiang, D.; Novoselov, K.; Roth, S.; Geim, A. K. Raman Spectrum of Graphene and Graphene Layers. *Phys. Rev. Lett.* **2006**, *97*, No. 187401.
(57) Radoń, A.; Włodarczyk, P.; Łukowiec, D. Structure, Temperature and Frequency Dependent Electrical Conductivity of Oxidized and Reduced Electrochemically Exfoliated Graphite. *Physica E Low Dimens. Syst. Nanostruct.* **2018**, *99*, 82−90.
(58) Kaniyoor, A.; Ramaprabhu, S. A Raman Spectroscopic Investigation of Graphite Oxide Derived Graphene. *AIP Adv.* **2012**, *2* (3), No. 032183.
(59) Ferrari, A. C.; Robertson, J. Interpretation of Raman Spectra of Disordered and Amorphous Carbon. *Phys. Rev. B* **2000**, *61* (20), 14095−14107.
(60) Cançado, L. G.; Jorio, A.; Ferreira, E. H. M.; Stavale, F.; Achete, C. A.; Capaz, R. B.; Moutinho, M. V. O.; Lombardo, A.; Kulmala, T. S.; Ferrari, A. C. Quantifying Defects in Graphene via Raman Spectroscopy at Different Excitation Energies. *Nano Lett.* **2011**, *11* (8), 3190−3196.
(61) Ma, B.; Rodriguez, R. D.; Ruban, A.; Pavlov, S.; Sheremet, E. The Correlation Between Electrical Conductivity and Second-Order Raman Modes of Laser-Reduced Graphene Oxide. *Phys. Chem. Chem. Phys.* **2019**, *21* (19), 10125−10134.
(62) Vollebregt, S.; Ishihara, R.; Hou, Y.; Beenakker, C. I. M. Influence of the Growth Temperature on the First and Second-Order Raman Band Ratios and Widths of Carbon Nanotubes and Fibers. *Carbon* **2012**, *50* (10), 3542−3554.
(63) López-Díaz, D.; López Holgado, M.; García-Fierro, J. L.; Velázquez, M. M. Evolution of the Raman Spectrum with the Chemical Composition of Graphene Oxide. *J. Phys. Chem. C* **2017**, *121* (37), 20489−20497.
(64) May, P.; Lazzeri, M.; Venezuela, P.; Herziger, F.; Callsen, G.; Reparaz, J. S.; Hoffmann, A.; Mauri, F.; Maultzsch, J. Signature of the Two-Dimensional Phonon Dispersion in Graphene Probed by Double-Resonant Raman Scattering. *Phys. Rev. B* **2013**, *87* (7), No. 075402.
(65) Robertson, J. Recombination and Photoluminescence Mechanism in Hydrogenated Amorphous Carbon. *Phys. Rev. B* **1996**, *53* (24), 16302−16305.
(66) Nanda, S. S.; Kim, M. J.; Yeom, K. S.; An, S. S. A.; Ju, H.; Yi, D. K. Raman Spectrum of Graphene with its Versatile Future Perspectives. *TrAC - Trends Anal. Chem.* **2016**, *80*, 125−131.
(67) Martins Ferreira, E. H.; Moutinho, M. V. O.; Stavale, F.; Lucchese, M. M.; Capaz, R. B.; Achete, C. A.; Jorio, A. Evolution of the Raman Spectra from Single-, Few-, and Many-Layer Graphene with Increasing Disorder. *Phys. Rev. B* **2010**, *82* (12), No. 125429.
(68) Ricciardella, F.; Massera, E.; Polichetti, T.; Miglietta, M. L.; Di Francia, G. A Calibrated Graphene-based Chemi-Sensor for Sub Parts-per-Million NO2 Detection Operating at Room Temperature. *Appl. Phys. Lett.* **2014**, *104* (18), No. 183502.
(69) Li, Z. Q.; Lu, C. J.; Xia, Z. P.; Zhou, Y.; Luo, Z. X-ray Diffraction Patterns of Graphite and Turbostratic Carbon. *Carbon* **2007**, *45* (8), 1686−1695, DOI: 10.1016/j.carbon.2007.03.038.
(70) Malard, L. M.; Pimenta, M. A.; Dresselhaus, G.; Dresselhaus, M. S. Raman Spectroscopy in Graphene. *Phys. Rep.* **2009**, *473* (5−6), 51−87.

https://doi.org/10.1021/acsomega.3c04788
ACS Omega 2023, 8, 40387−40395